

Article

Dissociation of State-Selected Ions Studied by Fixed-Photon-Energy Double-Imaging Photoelectron Photoion Coincidence: Cases of O_2^+ and CH_3F^+

Xiaofeng Tang ^{1,*} , Gustavo A. Garcia ² and Laurent Nahon ² 

¹ Laboratory of Atmospheric Physico-Chemistry, Anhui Institute of Optics and Fine Mechanics, HFIPS, Chinese Academy of Sciences, Hefei 230031, China

² Synchrotron SOLEIL, L'Orme des Merisiers, St. Aubin BP 48, 91192 Gif sur Yvette, France

* Correspondence: tangxf@aiofm.ac.cn

Abstract: This study presents the method of fixed-photon-energy double-imaging photoelectron photoion coincidence (i^2 PEPICO) utilized to investigate the dissociation of state-selected ions. Vacuum ultraviolet (VUV) synchrotron radiation at one fixed photon energy of $h\nu = 21.2$ eV, the He(I) atomic resonance energy, is employed as a light source to ionize molecules. Various dynamic information including time-of-flight (TOF) mass spectra, mass-selected photoelectron spectra (PES), and electron and ion kinetic energy correlation diagrams corresponding to each mass are obtained efficiently with the multiplexed capabilities of i^2 PEPICO, thereby revealing the detailed dissociation mechanisms of ions. As representative examples, dissociation of state-selected O_2^+ ions prepared in the $b^4\Sigma_g^-$ and $B^2\Sigma_g^-$ electronic states and CH_3F^+ ions in the X^2E , A^2A_1 , and B^2E states were selected and investigated.



Citation: Tang, X.; Garcia, G.A.; Nahon, L. Dissociation of State-Selected Ions Studied by Fixed-Photon-Energy Double-Imaging Photoelectron Photoion Coincidence: Cases of O_2^+ and CH_3F^+ . *Physchem* **2022**, *2*, 261–273. <https://doi.org/10.3390/physchem2030019>

Academic Editor: Ricardo Mosquera

Received: 7 May 2022

Accepted: 2 August 2022

Published: 5 August 2022

Publisher's Note: MDPI stays neutral with regard to jurisdictional claims in published maps and institutional affiliations.



Copyright: © 2022 by the authors. Licensee MDPI, Basel, Switzerland. This article is an open access article distributed under the terms and conditions of the Creative Commons Attribution (CC BY) license (<https://creativecommons.org/licenses/by/4.0/>).

Keywords: double imaging photoelectron photoion coincidence; oxygen; methyl fluoride; photoelectron spectrum; vacuum ultraviolet

1. Introduction

Vacuum ultraviolet (VUV) photoionization and dissociative photoionization of gas-phase molecules are fundamental photon–matter reactions in nature and have been the subject of numerous experimental and theoretical studies [1–3]. In the past few decades, photoelectron spectroscopy (PES) and photoionization mass spectrometry (PIMS) as universal analysis methods have provided valuable insight into molecular structure and chemical reactivity. Building on the established capabilities of PES [1] and PIMS [4,5], photoelectron photoion coincidence spectroscopy (PEPICO), based upon the detection of both electrons and ions in coincidence, can provide a complete picture of the photoionization and dissociative photoionization outcome. Moreover, the PEPICO scheme is also a powerful method to prepare and analyze state-selected cations.

A wealth of PEPICO techniques have been developed around pulsed sources, making use of their time structure to measure the 3D momentum of electrons and ions in coincidence and thereby allowing for an event-per-event full-vectorial correlation measurement [6–9]. However, the present study will focus only on the use of continuous light sources. Depending on the different photoionization light sources and electron analyzers used, two main PEPICO approaches have been implemented. (i) In earlier PEPICO applications, a relatively simple narrowband source such as a He(I) atomic discharge lamp at $h\nu = 21.2$ eV was used as photoionizing light source, and electrons with different kinetic energies were assessed with an electrostatic analyzer and measured in coincidence with ions [10,11]. (ii) A broadband continuum light source, such as an Ar or He Hopfield continuum discharge lamp and synchrotron radiation, is equipped with a VUV monochromator. This equipment is then used to scan through various ionic states, analyzing either all the

photoelectrons in coincidence with a given ion—to measure mass-tagged photoionization efficiency (PIE) curves [12] or angle-resolved constant-ionic-state (CIS) spectra [13,14]—or only near-zero kinetic energy electrons, commonly referred to as threshold photoelectrons, in the so-called threshold PEPICO (TPEPICO) scheme [15,16]. TPEPICO has the advantages of high collection efficiency and high-energy resolution for threshold photoelectrons, particularly when the strategy of electron velocity-map imaging (VMI) is used [17,18]. Another difference between TPEPICO and fixed-photon-energy PEPICO is that the former is especially sensitive to autoionizing resonances [12,19]. The rapid development of the third generation synchrotron facilities offer high-flux, high energy resolution and easily tuneable VUV photons in photoionization, which has led to TPEPICO becoming popular, especially among the chemistry-oriented community.

In recent years, the state-of-the-art method of double-imaging photoelectron–photoion coincidence (i^2 PEPICO), which employs double-imaging detection for both electrons and ions, has been utilized at several synchrotron facilities in the world, such as the Photon Factory [20], Hefei National Synchrotron Radiation Laboratory [21], SOLEIL synchrotron [22] and Swiss Light Source [23]. The i^2 PEPICO provides valuable information in various fields of physics and chemistry (for example, see section V of Ref. [16]). In particular, threshold photoelectron spectrum (TPES) and mass-selected TPES, corresponding to each mass with energy resolution down to the sub-meV level [24], can be obtained by scanning synchrotron photon energy and have the potential to identify transient and final products in chemical reactions [25–29]. However, the scanning is very time-consuming and usually needs several hours or even days to acquire a high resolution TPES. The long-time scanning is challenging in terms of light source and sample stability. In addition, the availability of synchrotron beamtime is very limited, and usually only a few days per year can be obtained for a given project.

In i^2 PEPICO setups, two position-sensitive detectors (PSDs) are installed to collect electrons and ions, respectively, and their 2D/3D momentum distributions can be unravelled through analysis of their images. As all the electrons with a specific range of kinetic energy are collected, threshold photoelectrons along with other energetic electrons can be detected and correlated to their corresponding ions in coincidence. In other words, i^2 PEPICO simultaneously combines the advantages of TPEPICO (high collection efficiency) and the earlier PEPICO (broad kinetic energy coverage) in a multiplex format. Therefore, when moderate electron energy resolution is sufficient for beamtime-limited experiments, it is not necessary to continuously scan the synchrotron photon energy since these experiments can be performed at just one or two fixed photon energies, while much information can be gathered given the multiplexed-capabilities of i^2 PEPICO [30]. Ion imaging also has the ability to measure kinetic energy release (KER) and angular distributions of ions correlating to definite electron binding energies [31], and to select a region of interest (ROI) in complex mixtures, such as the ones produced in a flow tube [25], in order to increase the detection dynamic range by removing the background. Fixed-photon-energy i^2 PEPICO can be operated with high efficiency, saving synchrotron beamtime, as demonstrated in the probing of sample mixtures [24], reaction intermediates, and isomers [32–34]. The emergence of new VUV/XUV light sources, either high repetition (>1 kHz) lasers [35] or lamps at fixed photon energy [36,37], makes table-top i^2 PEPICO experiments attractive and available.

In this work, we present an illustration of i^2 PEPICO at fixed photon energy to study the dissociation of state-selected ions. The experiments are performed at a single fixed photon energy, $h\nu = 21.2$ eV, and detailed dynamical information can be obtained owing to the multiplexed capabilities of i^2 PEPICO. As representative examples, the dissociation of state-selected O_2^+ ions, prepared in the $b^4\Sigma_g^-$ and $B^2\Sigma_g^-$ electronic states [8,38–40], and CH_3F^+ ions, in the X^2E , A^2A_1 and B^2E low-lying electronic states [31,41–43], have been selected for investigation. A large array of information on the dissociation, including photoionization time-of-flight (TOF) mass spectra, mass-selected PES, and electron and ion

kinetic energy correlation diagrams corresponding to each mass, are obtained efficiently and applied to reveal the dissociation mechanisms.

2. Materials and Methods

The experiments were carried out with an i^2 PEPICO spectrometer, DELICIOUS 3 [22], on the VUV beamline DESIRS [44] at synchrotron SOLEIL, France. The configuration of the i^2 PEPICO spectrometer installed inside the SAPHIRS permanent photoionization end-station has already been introduced in detail before [45], so only a brief description is presented here. As shown in Figure 1, the i^2 PEPICO spectrometer is composed of an electron VMI spectrometer, coupled to a modified Wiley–McLaren TOF 3D momentum ion-imaging analyzer, in order to measure electrons and ions in coincidence, owing to delay-line anode-based PSDs. Briefly, a VMI design has been applied on the electron side of the i^2 PEPICO spectrometer to collect electrons and analyze their kinetic energy and angular distribution. On the ion side, a modified Wiley–McLaren 3D momentum imaging spectrometer has been installed to measure the ion momentum vector event-by-event without the need for image inversion, presenting a good compromise between mass and kinetic energy resolution. In addition, by tuning the potentials on the two gridless electrodes located inside the second ion-acceleration region, one can change between momentum and space imaging, the latter being very helpful for molecular-beam alignment. The detailed voltage setting of these electrodes can be found in the literature [22]. A custom-made PSD (40 mm diameter) is placed at the end of the Wiley–McLaren TOF ion analyzer and a commercial PSD (Roentdek DLD80, 80 mm diameter) is installed on the electron side to collect electron signals. The eight electronic signals from the two PSDs, plus another two fast signals taken from the electron and ion multichannel plates (MCPs), are amplified, discriminated, and fed into a custom-made time-to-digital converter (TDC) for analysis. A multi-start/multi-stop (MS/MS) data acquisition scheme is used in coincidence to get a preferable signal-to-noise ratio and a random spread of false coincidences over the temporal window, providing a better noise subtraction [46].

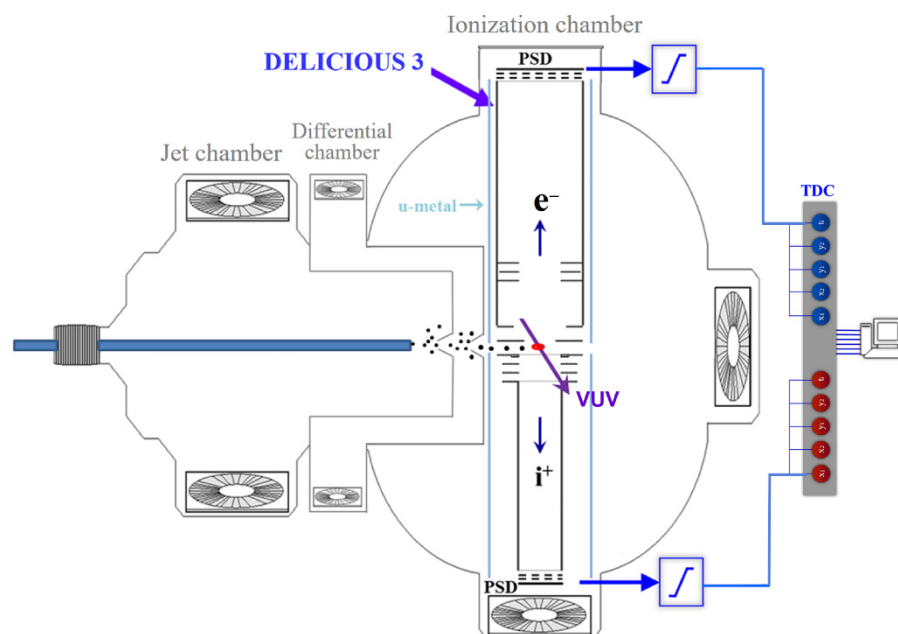


Figure 1. A schematic diagram of the experimental setup, including the i^2 PEPICO spectrometer and the jet, differential, and ionization chambers.

In our routine experiments, to get high-resolution energetic and spectroscopic information, TPES and mass-selected TPES (TPEPICO spectra) are measured by scanning synchrotron photon energy with a small step size and selecting only the threshold photoelectrons using a hot-electron subtraction method. The i^2 PEPICO scheme at fixed photon

energy can yield electron images correlated to a specific mass and 3D or 2D ion momentum. These filtered electron images are then processed by an Abel inversion algorithm [47] to recover mass-selected and KER-selected PES. The electron and ion kinetic energy correlation diagrams corresponding to each mass at fixed photon energy are obtained from the coincidence of photoelectron and ion images, and then the detailed dynamic information in dissociation can be acquired. After the upgrade of the SAPHIRS end-station [45], the electron kinetic energy resolution of the i^2 PEPICO spectrometer has been improved down to 2.8% ($\Delta E/E$) while the mass resolution reaches 1700 (mass 1700 and 1701 being separated at half-maximum of their peaks) with a repeller voltage of 500 V.

On the beamline, synchrotron radiation emitted from an undulator is dispersed by a 6.65 m normal-incidence monochromator used here with a 200 lines/mm grating. In the present experiments, the synchrotron photon energy is not scanned, and is fixed at $h\nu = 21.2$ eV. Commercial O_2 or CH_3F gas without further purification is expanded through a 50- μ m-diameter nozzle and traverse two 1.0-mm-diameter skimmers in the SAPHIRS end-station. The synchrotron photon beam, the molecular beam, and the axis of the i^2 PEPICO spectrometer are crossed at right angles in the photoionization region. The typical working pressures in the jet, differential, and ionization chambers of SAPHIRS are $\sim 10^{-3}$, 10^{-5} , and 10^{-6} Pa, respectively, with the continuous molecular beam on.

3. Dissociation of State-Selected O_2^+ Ion

Dissociative photoionization of oxygen, which has been studied by many groups before [8,38–40], is selected as a prototype to demonstrate the performances of i^2 PEPICO at fixed photon energy. The oxygen molecule belongs to the point group of $D_{\infty h}$ and its $X^3\Sigma_g^-$ ground state has an electron configuration of $(1\sigma_g)^2(1\sigma_u)^2(2\sigma_g)^2(2\sigma_u)^2(3\sigma_g)^2(1\pi_u)^4(1\pi_g)^2$. Due to the open-shell electron configuration, a great deal of ionic states of O_2^+ can be prepared and have been identified in the energy range of 12.0–21.2 eV. For example, the $b^4\Sigma_g^-$ and $B^2\Sigma_g^-$ electronic states are formed by the ejection of a $3\sigma_g$ outer-valence electron and these two states show a long vibrational progression in PES [8,39,40]. The adiabatic ionization energies of the $b^4\Sigma_g^-$ and $B^2\Sigma_g^-$ electronic states locate at 18.1713 and 20.2983 eV, respectively [48,49]. The high vibrational levels of the $b^4\Sigma_g^-$ state and the $B^2\Sigma_g^-$ electronic state are unstable and pre-dissociate to an O atom and an O^+ atomic ion fragments. Two dissociation limits of O_2^+ , $O^+(^4S) + O(^3P)$ at 18.733 eV and $O^+(^4S) + O(^1D)$ at 20.700 eV, are involved in the present energy range and have been identified in the dissociation [8,38–40].

3.1. Time-of-Flight Mass Spectrum and Ion Images

The TOF mass spectrum of O_2 is recorded at the fixed photon energy of $h\nu = 21.2$ eV and presented in Figure 2a, with 10-times-magnified data in blue. Two peaks at $m/z = 16$ and 32 are observed in the mass spectrum and assigned as the O^+ fragment ion and the O_2^+ parent ion, respectively. In contrast to the intense and sharp mass peak of the O_2^+ parent ion, the O^+ fragment ion peak has a wider width, reflecting a large kinetic energy released in the dissociation.

The ion images of the O_2^+ parent ion and the O^+ fragment ion are shown in Figure 2b,c. Due to the speed of the molecular beam, the ion images are slightly off-center on the detector. The propagation direction of the molecular beam is from east to west along the horizontal axis of the images. As most of the kinetic energy released in the photoionization of molecular oxygen has been carried away by the accompanied electrons, the O_2^+ parent ion appears as a small spot in the ion image due to the fine ion-velocity focusing of the i^2 PEPICO spectrometer [22]. In agreement with the wide peak of the mass spectrum, the O^+ fragment ion appears as a large pattern in the ion image of Figure 2c. In addition, in accordance with the two limits $O^+(^4S) + O(^3P)$ and $O^+(^4S) + O(^1D)$ involved in the dissociation, two concentric rings can be identified in the O^+ fragment ion image.

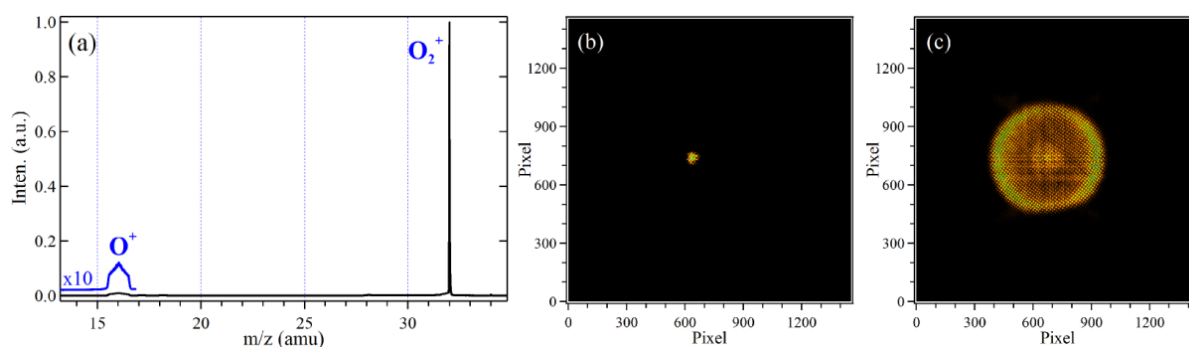


Figure 2. (a) Time-of-flight mass spectrum, (b) the O_2^+ parent ion image, and (c) the O^+ fragment ion image.

3.2. Mass-Selected Electron Images and Photoelectron Spectra

The mass-selected electron images corresponding to the O_2^+ parent ion and the O^+ fragment ion are shown in Figure 3a,c. The polarization of VUV photons is linear [44] and along the horizontal axis of the images. The upper-half portions of the electron images represent the raw data and the lower-halves correspond to the results from the pBasex Abel inversion algorithm [47]. Two main rings can be observed in the electron image of the O_2^+ parent ion along with some weaker structures. The electron image of the O^+ fragment ion has much richer structures, as illustrated by the number of concentric rings that can be clearly identified.

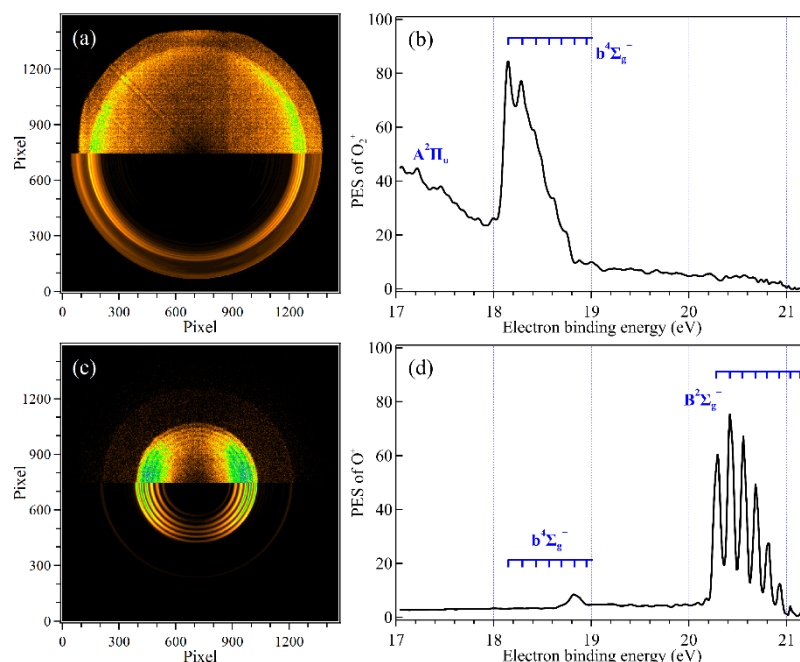


Figure 3. Mass-selected electron images and their corresponding photoelectron spectra, (a,b) the O_2^+ parent ion, (c,d) the O^+ fragment ion.

The mass-selected PES corresponding to the O_2^+ parent and the O^+ fragment ions obtained from the two electron images are presented in Figure 3b,d, respectively. The extraction electric field of the i^2 PEPICO spectrometer was set at 104 V/cm, and under these experimental conditions, the electrons with kinetic energy of less than ~ 4.2 eV can be mapped on the electron PSD and detected without discrimination. One can see that in the electron binding energy range of 17.0–21.2 eV, three electronic states of O_2^+ have been populated with the present photons and are assigned in the PES. The $A^2\Pi_u$ electronic state is stable and can be observed in the mass-selected PES of the O_2^+ parent ion. However, due

to the limitation of the electron kinetic energy resolution for fast electrons, the vibrational series of the $A^2\Pi_u$ electronic state are not resolved in the PES. At $h\nu = 21.2$ eV, the electrons emitted from the $A^2\Pi_u$ electronic state can take 3–4 eV kinetic energies, and their absolute energy resolution is about 0.2 eV (a slight dependent on the electron kinetic energy), which is larger than the vibrational spacing (0.07–0.11 eV) of the $A^2\Pi_u$ electronic state [45,50]. The lower vibrational levels of the $b^4\Sigma_g^-$ electronic state are stable and show some partially resolved vibrational structures in the PES of Figure 3b. With the increase of the electron-binding energy, the electron signals of the O_2^+ parent ion disappear at ~ 18.8 eV in Figure 3b.

The electron signals of the O^+ fragment ion appear at ~ 18.7 eV in the PES of Figure 3d, implying that high vibrational levels of the $b^4\Sigma_g^-$ state are unstable and dissociate into the O and O^+ fragments. In the electron binding energy range of 20.2–21.2 eV, several peaks can be observed in the PES and are assigned to the $v = 0$ –6 vibrational progressions of the $B^2\Sigma_g^-$ state, as consistent with previous findings [8,38–40].

As discussed above, the vibrational levels of the $b^4\Sigma_g^-$ electronic state are not clearly discerned in the PES due to the limited electron kinetic energy resolution for fast electrons. This problem could be overcome by reducing the electron kinetic energy to increase the absolute energy resolution. For example, after changing the synchrotron photon energy down to $h\nu = 19.2$ eV, the vibrational structures of the $b^4\Sigma_g^-$ electronic state can be clearly determined, and assigned in the images and PES as depicted in Figure 4. The present results clearly show that the $v = 0$ –3 vibrational levels of the $b^4\Sigma_g^-$ state are stable, the $v = 5$ –7 vibrational levels totally dissociate into the $O^+(^4S)$ and $O(^3P)$ fragments, and the $v = 4$ vibrational level is partially dissociative, according well with previous data [8,38]. Note that the choice of the photon energy is important in the fixed-photon-energy i^2 PEPICO experiments because of the compromise between kinetic energy resolution and bandwidth. Indeed, with 4π transmission analyzers the absolute resolution degrades for faster particles so that several small-energy windows, i.e., photon energies, might be more advantageous than a single large-energy window covering several states if the ionization source is easily tuneable. An extrapolation of this concept is threshold photoelectron spectroscopy, where the spectrometer bandwidth is narrow and the photon source is continuously tuned [16].

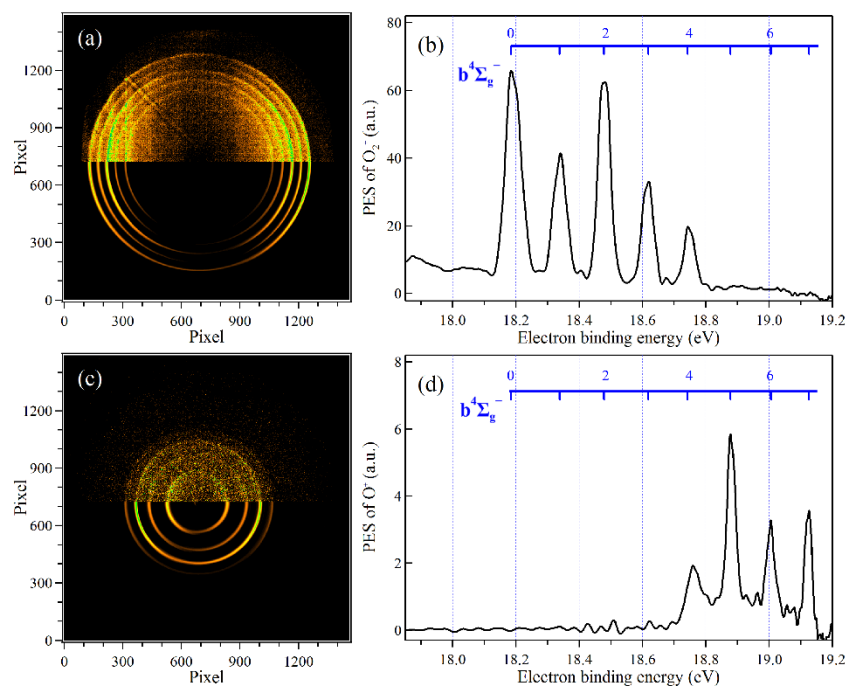


Figure 4. Mass-selected electron images and their corresponding photoelectron spectra, (a,b) the O_2^+ parent ion, (c,d) the O^+ fragment ion, recorded at $h\nu = 19.2$ eV.

3.3. Electron and Ion Kinetic Energy Correlation Diagrams

The electron images and the ion images can be correlated together in coincidence to obtain detailed dynamic information on the photoionization and dissociative photoionization. The electron and ion kinetic energy correlation diagrams corresponding to the O_2^+ parent ion and the O^+ fragment ion obtained from the images of Figures 2 and 3 are presented in Figure 5a,b, respectively, in which their individual KER distributions can be acquired. The O_2^+ parent ions are stable in the $A^2\Pi_u$ electronic state and the lower vibrational levels of the $b^4\Sigma_g^-$ state.

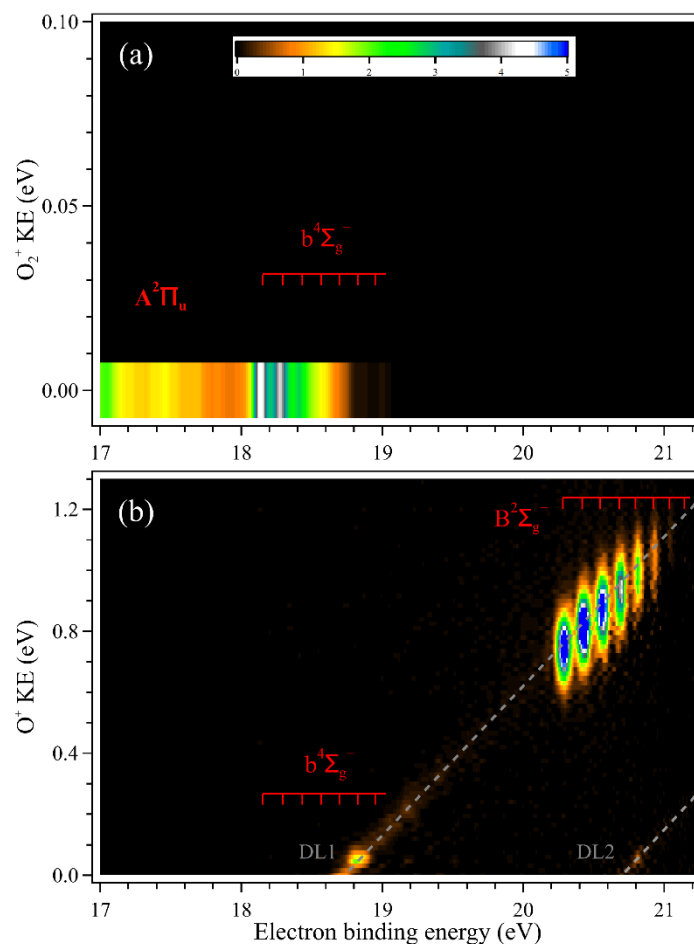


Figure 5. Electron and ion kinetic energy correlation diagram corresponding to (a) the O_2^+ parent ion and (b) the O^+ fragment ion, with the assignments along the $O^+(^4S) + O(^3P)$ and $O^+(^4S) + O(^1D)$ dissociation channels. As shown in the inserted color panel, the ion signal intensity increases from orange to white then blue, with black representing zero.

In Figure 5b, the vibrational levels of the $b^4\Sigma_g^-$ and $B^2\Sigma_g^-$ electronic states, together with the dissociation along the first dissociation limit $O^+(^4S) + O(^3P)$, DL1, and the second dissociation limit $O^+(^4S) + O(^1D)$, DL2 [8,38–40], have been assigned in the correlation diagram of the O^+ fragment ion. It is shown that the O^+ fragment ion firstly appears at the $v = 4$ vibrational level of the $b^4\Sigma_g^-$ electronic state, and then its kinetic energy increases linearly along the diagonal line of the first dissociation limit DL1, as well as within the energy range of the $B^2\Sigma_g^-$ electronic state.

The vibrational levels of the $B^2\Sigma_g^-$ electronic state are clearly identified in the correlation diagram of Figure 5b and the dissociation of O_2^+ ion towards the second dissociation limit DL2 appears at the $v = 4$ vibrational level of the $B^2\Sigma_g^-$ state. We can see that the dissociation of O_2^+ in the $B^2\Sigma_g^-$ state is mainly towards the first dissociation limit $O^+(^4S) + O(^3P)$ and the branching ratio of the products towards the second dissociation

limit $O^+(^4S) + O(^1D)$ is small. The detailed mechanism involved in the dissociation of state-selected O_2^+ ions can be revealed with the aid of dynamics information, as described in detail in previous publications [8,38–40], in which predissociation via several dissociative states has been determined.

4. Dissociation of State-Selected CH_3F^+ Ion

The method of fixed-photon-energy i^2 PEPICO has also been utilized to investigate dissociation of state-selected CH_3F^+ ions. Methyl fluoride has a C_{3v} high symmetry and its electron configuration in the neutral ground electronic state is $(1a_1)^2(2a_1)^2(1e)^4(3a_1)^2(2e)^4$. Three low-lying electronic states of CH_3F^+ , X^2E , A^2A_1 , and B^2E , can be prepared after removing an electron from the three outer valence orbitals, $2e$, $3a_1$, and $1e$, respectively, in the photoionization with VUV photons of $h\nu = 21.2$ eV. In addition, the dissociation of the CH_3F^+ ion is of fundamental interest and undergoes specific reactions into different products depending on the ion's electronic states.

4.1. Time-of-Flight Mass Spectrum and Ion Images

The photoionization TOF mass spectrum of CH_3F recorded at the fixed photon energy of $h\nu = 21.2$ eV is presented in Figure 6a. In addition to the most intense peak of the CH_3F^+ parent ion at $m/z = 34$, the CH_3^+ ($m/z = 15$) and CH_2F^+ ($m/z = 33$) fragment ion peaks can be clearly observed in the mass spectrum. The peak width of the CH_3^+ fragment ion is much wider than that of the CH_3F^+ parent ion due to the large kinetic energy released in the dissociation. In addition, in agreement with our previous results [31,43], the CH_2^+ ($m/z = 14$) and CHF^+ ($m/z = 32$) fragment ions with weak signals are identified in the mass spectrum as well. The mass peak at $m/z = 35$ represents $\sim 1\%$ of the CH_3F^+ peak and is identified as the $^{13}CH_3F^+$ isotopic parent ion.

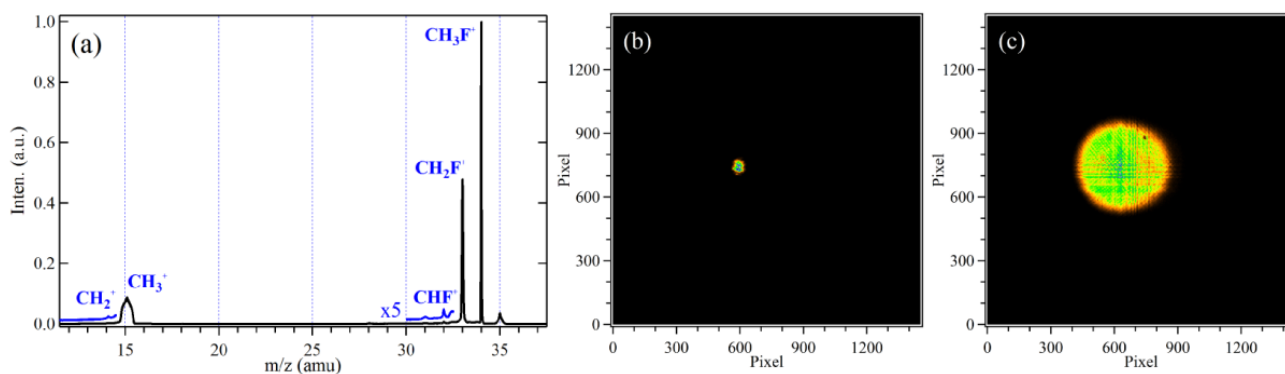


Figure 6. (a) Photoionization time-of-flight mass spectrum of CH_3F , with 5-times-magnified data in blue, (b) the CH_3F^+ parent ion image, and (c) the CH_3^+ fragment ion image.

The images of the CH_3F^+ parent ion and the CH_3^+ fragment ion are measured and shown in Figure 6b,c. The CH_3F^+ parent ion exhibits a small off-centered focused spot. In accordance with the wide peak of the CH_3^+ fragment ion in the mass spectrum, the CH_3^+ fragment ion image exhibits a large diameter, implying a large kinetic energy released in the dissociation.

4.2. Mass-Selected Electron Images and Photoelectron Spectra

The total photoelectron image and PES corresponding to all the ions involved in the photoionization are presented in Figure 7a,b. As shown in the PES, the three low-lying electronic states of CH_3F^+ , X^2E , A^2A_1 and B^2E , have been prepared with $h\nu = 21.2$ eV and assigned. Due to the small energy gap and their natural peak widths, the A^2A_1 and B^2E electronic excited states fully overlap and appear as a broad band in the PES.

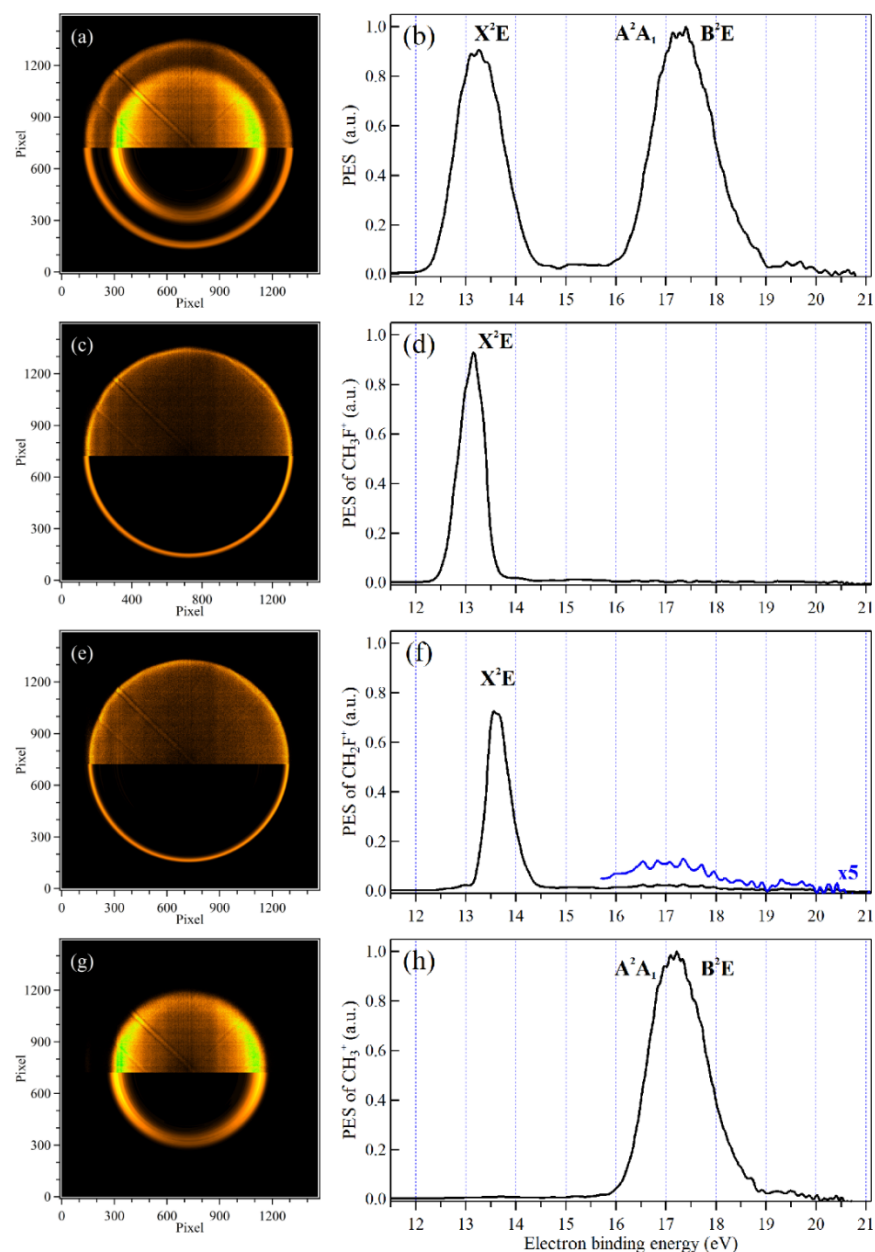


Figure 7. Mass-selected electron images and photoelectron spectra corresponding to (a,b) all ions, (c,d) the CH_3F^+ parent ion, (e,f) the CH_2F^+ fragment ion, and (g,h) the CH_3^+ fragment ion, with 5-times-magnified data in blue, partially adapted with permission from Ref. [43]. Copyright 2017 American Chemical Society.

The mass-selected electron images and PES corresponding to the CH_3F^+ parent ion, the CH_2F^+ fragment ion and the CH_3^+ fragment ion are shown in Figure 7 as well. In the mass-selected PES of Figure 7d, the CH_3F^+ parent ion is populated only in the low-energy part of the X^2E ground state, indicating that its high vibrational levels and the A^2A_1 and B^2E excited states are dissociative. The CH_3F^+ parent ions prepared at the high vibrational levels of the X^2E ground state dissociate to the CH_2F^+ and H fragments, as shown in the mass-selected PES of CH_2F^+ in Figure 7f. In addition, the CH_3F^+ parent ions prepared in the electron binding energy range of 16–19 eV can dissociate to the CH_2F^+ and H fragments as well, with a small branching ratio. The A^2A_1 and B^2E electronic states in the electron binding energy range of 16–19 eV are fully dissociative and their intensity in the mass-selected PES of CH_3^+ is almost the same as that in the total PES, indicating that the CH_3F^+ parent ions prepared in the A^2A_1 and B^2E electronic states primarily dissociate

to the CH_3^+ and F fragments. The signals of the CH_2^+ and CHF^+ fragment ions are so weak that their mass-selected electron images and PES (not shown here) are too noisy to provide any valuable information in the dissociation.

4.3. Electron and Ion Kinetic Energy Correlation Diagrams

The corresponding electron and ion kinetic energy correlation diagrams for the CH_3F^+ parent ion, the CH_2F^+ and CH_3^+ fragment ions are shown in Figure 8. The CH_3F^+ parent ions with almost zero kinetic energy are populated and stable in the low vibrational levels of the X^2E ground state. In the correlation diagram of Figure 8b, the CH_2F^+ fragment ions are produced in the high vibrational levels of the X^2E ground state, covering the electron binding energy range of 13–14 eV. As most of the kinetic energy released in the dissociation has already been removed by the accompanying H fragment, the kinetic energy of the CH_2F^+ fragment ion is quite small, slightly broader than that of the CH_3F^+ parent ion in Figure 8a.

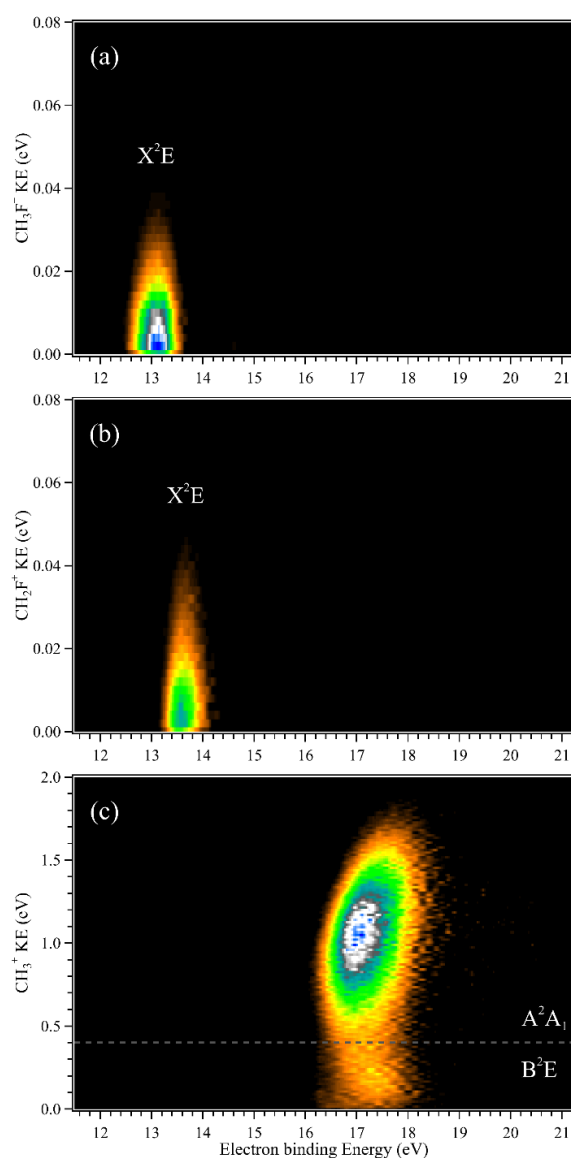


Figure 8. Electron and ion kinetic energy correlation diagrams corresponding to (a) the CH_3F^+ parent ion, (b) the CH_2F^+ fragment ion, and (c) the CH_3^+ fragment ion. Panel (c) is adapted with permission from Ref. [43]. Copyright 2017 American Chemical Society.

In Figure 8c, the A^2A_1 and B^2E electronic states overlap in the electron binding energy range of 16–19 eV and exhibit a large kinetic energy released in the dissociation. In the correlation diagram, the contour of the kinetic energy can be divided into two parts from the dissociation of the A^2A_1 and B^2E electronic states, respectively. The CH_3^+ fragment ion dissociated from the A^2A_1 state takes a large kinetic energy, whereas the released kinetic energy from the B^2E state is small, in agreement with their different dissociation mechanisms. Previous studies have shown that the A^2A_1 electronic state is a repulsive and directly dissociative state to produce CH_3^+ and F fragments, but in the B^2E state, the CH_3F^+ ions firstly perform internal conversion to the high vibrational levels of the X^2E ground state and then statistically dissociate to the CH_3^+ and F fragments [31,43].

5. Conclusions

The state-of-the-art method of double-imaging photoelectron photoion coincidence (i^2 PEPICO) at a fixed photon energy has been efficiently utilized to investigate dissociation dynamics of state-selected ions. The present experiments are mainly performed at only one fixed photon energy, $h\nu = 21.2$ eV, the He(I) atomic resonant energy, and a great deal of information in the dissociation has been acquired with the multiplex capabilities of i^2 PEPICO. As representative examples, dissociation of state-selected O_2^+ ions in the $b^4\Sigma_g^-$ and $B^2\Sigma_g^-$ electronic states and CH_3F^+ ions in the X^2E , A^2A_1 , and B^2E electronic states have been studied. The data of these two fixed-photon-energy i^2 PEPICO experiments were accumulated for only 3~4 h, respectively, and their detailed dissociation mechanisms can be revealed efficiently from the obtained experimental data such as the mass-selected PES and the electron and ion kinetic energy correlation diagrams corresponding to each mass. The limitations of fixed-photon-energy i^2 PEPICO, especially the electron kinetic energy resolution, have also been discussed, and some upgrade schemes will be taken into account in future experiments. As demonstrated by the present work, the i^2 PEPICO experiments can be combined with other light sources, not only to the tuneable synchrotron radiation, but also to VUV/XUV laser sources based upon 4-wave mixing and high-harmonic generation (HHG), as well as modern VUV discharge lamps and excimer sources. In addition, the advances of the i^2 PEPICO technique, such as the background removal leading to a high signal-to-noise ratio and the dynamical range enhancement [28], have the analytical potential to detect elusive species with electronic fingerprints to decipher isomers [34,51] and will provide new insights into in situ and real-time analysis of chemical reactions.

Author Contributions: Formal analysis, L.N.; Investigation, G.A.G.; Investigation, Writing—original draft, X.T. All authors have read and agreed to the published version of the manuscript.

Funding: X.T. would like to thank supporters from the National Natural Science Foundation of China (91961123, 42120104007), the Chinese Academy of Sciences (116134KYSB20170048) and the Key Program of Research and Development of Hefei Science Center, CAS (No. 2020HSCKPRD001).

Institutional Review Board Statement: Not applicable.

Informed Consent Statement: Not applicable.

Data Availability Statement: The data that support the finding of this study are available from the corresponding author upon reasonable request.

Acknowledgments: The authors are grateful to the SOLEIL general staff for running the synchrotron facility and providing beamtime under project 20210072.

Conflicts of Interest: The authors declare no conflict of interest.

References

1. Eland, J.H.D. *Photoelectron Spectroscopy: An Introduction to Ultraviolet Photoelectron Spectroscopy in the Gas Phase*; Butterworths: London, UK, 1984.
2. Baer, T.; Hase, W.L. *Unimolecular Reaction Dynamics: Theory and Experiments*; Oxford University Press: Oxford, UK, 1996.
3. Ng, C.Y. Vacuum ultraviolet spectroscopy and chemistry by photoionization and photoelectron methods. *Annu. Rev. Phys. Chem.* **2002**, *53*, 101–140. [[CrossRef](#)] [[PubMed](#)]

4. Qi, F. Combustion chemistry probed by synchrotron VUV photoionization mass spectrometry. *Proc. Combust. Inst.* **2013**, *34*, 33–63. [[CrossRef](#)]
5. Kostko, O.; Bandyopadhyay, B.; Ahmed, M. Vacuum ultraviolet photoionization of complex chemical systems. *Annu. Rev. Phys. Chem.* **2016**, *67*, 19–40. [[CrossRef](#)] [[PubMed](#)]
6. Lafosse, A.; Lebech, M.; Brenot, J.C.; Guyon, P.M.; Jagutzki, O.; Spielberger, L.; Vervloet, M.; Houver, J.C.; Doweck, D. Vector correlations in dissociative photoionization of diatomic molecules in the VUV range: Strong anisotropies in electron emission from spatially oriented NO molecules. *Phys. Rev. Lett.* **2000**, *84*, 5987–5990. [[CrossRef](#)]
7. Lebech, M.; Houver, J.C.; Doweck, D. Ion–electron velocity vector correlations in dissociative photoionization of simple molecules using electrostatic lenses. *Rev. Sci. Instrum.* **2002**, *73*, 1866–1874. [[CrossRef](#)]
8. Jarvis, G.K.; Weitzel, K.M.; Malow, M.; Baer, T.; Song, Y.; Ng, C.Y. High-resolution pulsed field ionization photoelectron-photoion coincidence spectroscopy using synchrotron radiation. *Rev. Sci. Instrum.* **1999**, *70*, 3892–3906. [[CrossRef](#)]
9. Jahnke, T.; Weber, T.; Osipov, T.; Landers, A.L.; Jagutzki, O.; Schmidt, L.P.H.; Cocke, C.L.; Prior, M.H.; Schmidt-Bocking, H.; Dorner, R. Multicoincidence studies of photo and Auger electrons from fixed-in-space molecules using the COLTRIMS technique. *J. Electron Spectrosc. Relat. Phenom.* **2004**, *141*, 229–238. [[CrossRef](#)]
10. Eland, J.H.D. Coincidence studies of multiionized molecules. In *Vacuum Ultraviolet Photoionization and Photodissociation of Molecules and Clusters*; Ng, C.Y., Ed.; World Scientific: Singapore, 1991; pp. 297–344.
11. Eland, J.H.D. Photoelectron-photoion coincidence spectroscopy. I. Basic principles and theory. *Int. J. Mass Spectrom. Ion Phys.* **1972**, *8*, 143–151. [[CrossRef](#)]
12. Brechignac, P.; Garcia, G.A.; Falvo, C.; Joblin, C.; Kokkin, D.; Bonnamy, A.; Parneix, P.; Pino, T.; Pirali, O.; Mulas, G.; et al. Photoionization of cold gas phase coronene and its clusters: Autoionization resonances in monomer, dimer, and trimer and electronic structure of monomer cation. *J. Chem. Phys.* **2014**, *141*, 164325. [[CrossRef](#)]
13. Chartrand, A.M.; McCormack, E.F.; Jacovella, U.; Holland, D.M.P.; Gans, B.; Tang, X.; Garcia, G.A.; Nahon, L.; Pratt, S.T. Photoelectron angular distributions from rotationally resolved autoionizing states of N₂⁺. *J. Chem. Phys.* **2017**, *147*, 224303. [[CrossRef](#)]
14. Holland, D.M.P.; Seddon, E.A.; Daly, S.; Alcaraz, C.; Romanzin, C.; Nahon, L.; Garcia, G.A. The effect of autoionization on the N₂⁺ X²S_g⁺ state vibrationally resolved photoelectron anisotropy parameters and branching ratios. *J. Phys. B At. Mol. Opt. Phys.* **2013**, *46*, 095102. [[CrossRef](#)]
15. Baer, T. State selection by photoion-photoelectron coincidence. In *Gas Phase Ion Chemistry*; Bowers, M.T., Ed.; Academic Press: New York, NY, USA, 1979; Volume 1, pp. 153–196.
16. Baer, T.; Tuckett, R.P. Advances in threshold photoelectron spectroscopy (TPES) and threshold photoelectron photoion coincidence (TPEPICO). *Phys. Chem. Chem. Phys.* **2017**, *19*, 9698–9723. [[CrossRef](#)] [[PubMed](#)]
17. Eppink, A.; Parker, D.H. Velocity map imaging of ions and electrons using electrostatic lenses: Application in photoelectron and photofragment ion imaging of molecular oxygen. *Rev. Sci. Instrum.* **1997**, *68*, 3477–3484. [[CrossRef](#)]
18. Sztaray, B.; Baer, T. Suppression of hot electrons in threshold photoelectron photoion coincidence spectroscopy using velocity focusing optics. *Rev. Sci. Instrum.* **2003**, *74*, 3763–3768. [[CrossRef](#)]
19. Briant, M.; Poisson, L.; Hochlaf, M.; de Pujo, P.; Gaveau, M.-A.; Soep, B. Ar₂ Photoelectron Spectroscopy Mediated by Autoionizing States. *Phys. Rev. Lett.* **2012**, *109*, 193401. [[CrossRef](#)]
20. Hosaka, K.; Adachi, J.; Golovin, A.V.; Takahashi, M.; Watanabe, N.; Yagishita, A. Coincidence velocity imaging apparatus for study of angular correlations between photoelectrons and photofragments. *Jpn. J. Appl. Phys.* **2006**, *45*, 1841–1849. [[CrossRef](#)]
21. Tang, X.; Zhou, X.G.; Niu, M.L.; Liu, S.L.; Sun, J.D.; Shan, X.B.; Liu, F.Y.; Sheng, L.S. A threshold photoelectron-photoion coincidence spectrometer with double velocity imaging using synchrotron radiation. *Rev. Sci. Instrum.* **2009**, *80*, 113101. [[CrossRef](#)]
22. Garcia, G.A.; de Miranda, B.K.C.; Tia, M.; Daly, S.; Nahon, L. DELICIOUS III: A multipurpose double imaging particle coincidence spectrometer for gas phase vacuum ultraviolet photodynamics studies. *Rev. Sci. Instrum.* **2013**, *84*, 053112. [[CrossRef](#)]
23. Bodi, A.; Hemberger, P.; Gerber, T.; Sztaray, B. A new double imaging velocity focusing coincidence experiment: i²PEPICO. *Rev. Sci. Instrum.* **2012**, *83*, 083105. [[CrossRef](#)]
24. Garcia, G.A.; Soldi-Lose, H.; Nahon, L. A versatile electron-ion coincidence spectrometer for photoelectron momentum imaging and threshold spectroscopy on mass selected ions using synchrotron radiation. *Rev. Sci. Instrum.* **2009**, *80*, 023102. [[CrossRef](#)]
25. Garcia, G.A.; Tang, X.; Gil, J.F.; Nahon, L.; Ward, M.; Batut, S.; Fittschen, C.; Taatjes, C.A.; Osborn, D.L.; Loison, J.C. Synchrotron-based double imaging photoelectron/photoion coincidence spectroscopy of radicals produced in a flow tube: OH and OD. *J. Chem. Phys.* **2015**, *142*, 164201. [[CrossRef](#)]
26. Zhu, Y.; Wu, X.; Tang, X.; Wen, Z.; Liu, F.; Zhou, X.; Zhang, W. Synchrotron threshold photoelectron photoion coincidence spectroscopy of radicals produced in a pyrolysis source: The methyl radical. *Chem. Phys. Lett.* **2016**, *664*, 237–241. [[CrossRef](#)]
27. Tang, X.; Lin, X.; Zhu, Y.; Wu, X.; Wen, Z.; Zhang, L.; Liu, F.; Gu, X.; Zhang, W. Pyrolysis of n-butane investigated using synchrotron threshold photoelectron photoion coincidence spectroscopy. *RSC Adv.* **2017**, *7*, 28746–28753. [[CrossRef](#)]
28. Sztaray, B.; Voronova, K.; Torma, K.G.; Covert, K.J.; Bodi, A.; Hemberger, P.; Gerber, T.; Osborn, D.L. CRF-PEPICO: Double velocity map imaging photoelectron photoion coincidence spectroscopy for reaction kinetics studies. *J. Chem. Phys.* **2017**, *147*, 013944. [[CrossRef](#)]

29. Tang, X.; Gu, X.; Lin, X.; Zhang, W.; Garcia, G.A.; Fittschen, C.; Loison, J.-C.; Voronova, K.; Sztaray, B.; Nahon, L. Vacuum ultraviolet photodynamics of the methyl peroxy radical studied by double imaging photoelectron photoion coincidences. *J. Chem. Phys.* **2020**, *152*, 104301. [[CrossRef](#)]
30. Felsmann, D.; Lucassen, A.; Kruger, J.; Hemken, C.; Tran, L.-S.; Pieper, J.; Garcia, G.A.; Brockhinke, A.; Nahon, L.; Kohse-Hoinghaus, K. Progress in fixed-photon-energy time-efficient double imaging photoelectron/photoion coincidence measurements in quantitative flame analysis. *Z. Phys. Chem.* **2016**, *230*, 1067–1097. [[CrossRef](#)]
31. Tang, X.; Garcia, G.A.; Nahon, L. CH_3^+ formation in the dissociation of energy-selected CH_3F^+ studied by double imaging electron/ion coincidences. *J. Phys. Chem. A* **2015**, *119*, 5942–5950. [[CrossRef](#)]
32. Bodi, A.; Hemberger, P.; Osborn, D.L.; Sztaray, B. Mass-resolved isomer-selective chemical analysis with imaging photoelectron photoion coincidence spectroscopy. *J. Phys. Chem. Lett.* **2013**, *4*, 2948–2952. [[CrossRef](#)]
33. Kruger, J.; Garcia, G.A.; Felsmann, D.; Moshhammer, K.; Lackner, A.; Brockhinke, A.; Nahon, L.; Kohse-Hoinghaus, K. Photoelectron-photoion coincidence spectroscopy for multiplexed detection of intermediate species in a flame. *Phys. Chem. Chem. Phys.* **2014**, *16*, 22791–22804. [[CrossRef](#)]
34. Pieper, J.; Schmitt, S.; Hemken, C.; Davies, E.; Wullenkord, J.; Brockhinke, A.; Krueger, J.; Garcia, G.A.; Nahon, L.; Lucassen, A.; et al. Isomer identification in flames with double imaging photoelectron/photoion coincidence spectroscopy ($i^2\text{PEPICO}$) using measured and calculated reference photoelectron spectra. *Z. Phys. Chem.* **2018**, *232*, 153–187. [[CrossRef](#)]
35. Fanood, M.M.R.; Ram, N.B.; Lehmann, C.S.; Powis, I.; Janssen, M.H.M. Enantiomer-specific analysis of multi-component mixtures by correlated electron imaging-ion mass spectrometry. *Nat. Commun.* **2015**, *6*, 7511. [[CrossRef](#)] [[PubMed](#)]
36. Muhlberger, F.; Wieser, J.; Ulrich, A.; Zimmermann, R. Single photon ionization (SPI) via incoherent VUV-excimer light: Robust and compact time-of-flight mass spectrometer for on-line, real-time process gas analysis. *Anal. Chem.* **2002**, *74*, 3790–3801. [[CrossRef](#)] [[PubMed](#)]
37. Wang, J.S.; Ritterbusch, F.; Dong, X.Z.; Gao, C.; Li, H.; Jiang, W.; Liu, S.Y.; Lu, Z.T.; Wang, W.H.; Yang, G.M.; et al. Optical Excitation and Trapping of ^{81}Kr . *Phys. Rev. Lett.* **2021**, *127*, 023201. [[CrossRef](#)]
38. Akahori, T.; Morioka, Y.; Watanabe, M.; Hayaishi, T.; Ito, K.; Nakamura, M. Dissociation processes of O_2 in the VUV region 500–700 Å. *J. Phys. B At. Mol. Opt. Phys.* **1985**, *18*, 2219–2229. [[CrossRef](#)]
39. Richardviard, M.; Dutuit, O.; Lavollee, M.; Govers, T.; Guyon, P.M.; Durup, J. O_2^+ ions dissociation studied by threshold photoelectron-photoion coincidence method. *J. Chem. Phys.* **1985**, *82*, 4054–4063. [[CrossRef](#)]
40. Tang, X.; Zhou, X.G.; Niu, M.L.; Liu, S.L.; Sheng, L.S. Dissociation of vibrational state-selected O_2^+ ions in the $\text{B}^2\Sigma_g$ state using threshold photoelectron-photoion coincidence velocity imaging. *J. Phys. Chem. A* **2011**, *115*, 6339–6346. [[CrossRef](#)] [[PubMed](#)]
41. Eland, J.H.D.; Frey, R.; Kuestler, A.; Schulte, H.; Brehm, B. Unimolecular dissociations and internal conversions of methyl halide ions. *Int. J. Mass Spectrom. Ion Phys.* **1976**, *22*, 155–170. [[CrossRef](#)]
42. Weitzel, K.M.; Guthe, F.; Mahnert, J.; Loch, R.; Baumgartel, H. Statistical and non-statistical reactions in energy selected fluoromethane ions. *Chem. Phys.* **1995**, *201*, 287–298. [[CrossRef](#)]
43. Tang, X.; Garcia, G.A.; Nahon, L. Double imaging photoelectron photoion coincidence sheds new light on the dissociation of state-selected CH_3F^+ ions. *J. Phys. Chem. A* **2017**, *121*, 5763–5772. [[CrossRef](#)]
44. Nahon, L.; de Oliveira, N.; Garcia, G.A.; Gil, J.F.; Pilette, B.; Marcouille, O.; Lagarde, B.; Polack, F. DESIRS: A state-of-the-art VUV beamline featuring high resolution and variable polarization for spectroscopy and dichroism at SOLEIL. *J. Synchrotron Rad.* **2012**, *19*, 508–520. [[CrossRef](#)]
45. Tang, X.; Garcia, G.A.; Gil, J.-F.; Nahon, L. Vacuum upgrade and enhanced performances of the double imaging electron/ion coincidence end-station at the vacuum ultraviolet beamline DESIRS. *Rev. Sci. Instrum.* **2015**, *86*, 123108. [[CrossRef](#)]
46. Bodi, A.; Sztaray, B.; Baer, T.; Johnson, M.; Gerber, T. Data acquisition schemes for continuous two-particle time-of-flight coincidence experiments. *Rev. Sci. Instrum.* **2007**, *78*, 084102. [[CrossRef](#)]
47. Garcia, G.A.; Nahon, L.; Powis, I. Two-dimensional charged particle image inversion using a polar basis function expansion. *Rev. Sci. Instrum.* **2004**, *75*, 4989–4996. [[CrossRef](#)]
48. Evans, M.; Stimson, S.; Ng, C.Y.; Hsu, C.W.; Jarvis, G.K. Rotationally resolved pulsed field ionization photoelectron study of $\text{O}_2+(\text{B}^2\Sigma_g^-, 2\Sigma_u^-; v^+ = 0-7)$ at 20.2–21.3 eV. *J. Chem. Phys.* **1999**, *110*, 315. [[CrossRef](#)]
49. Hsu, C.-W.; Heimann, P.; Evans, M.; Stimson, S.; Fenn, P.T.; Ng, C.Y. A high resolution pulsed field ionization photoelectron study of O_2 using third generation undulator synchrotron radiation. *J. Chem. Phys.* **1997**, *106*, 8931–8934. [[CrossRef](#)]
50. Song, Y.; Evans, M.; Ng, C.Y.; Hsu, C.-W.; Jarvis, G.K. Rotationally resolved pulsed-field ionization photoelectron bands for $\text{O}_2+(\text{A}^2\Pi_u, v^+ = 0-12)$ in the energy range of 17.0–18.2 eV. *J. Chem. Phys.* **2000**, *112*, 1271–1278. [[CrossRef](#)]
51. Nagaraju, S.; Tranter, R.S.; Ardila, F.E.C.; Abid, S.; Lynch, P.T.; Garcia, G.A.; Gil, J.F.; Nahon, L.; Chaumeix, N.; Comandini, A. Pyrolysis of ethanol studied in a new high-repetition-rate shock tube coupled to synchrotron-based double imaging photoelectron/photoion coincidence spectroscopy. *Combust. Flame* **2021**, *226*, 53–68. [[CrossRef](#)]